Journal of
MATERIALS
RESEARCH

SiC (SCS-6) fiber reinforced–reaction formed SiC matrix composites: Microstructure and interfacial properties

M. Singh and R. M. Dickerson
NYMA, Inc., Lewis Research Center Group, Cleveland, Ohio 44135

Forrest A. Olmstead
Department of Mechanical Engineering, Case Western Reserve University, Cleveland, Ohio 44106

J. I. Eldridge
NASA Lewis Research Center, Cleveland, Ohio 44135

pp. 706-713

Volume 12, Number 3
March 1997

Published by the Materials Research Society

SiC (SCS-6) fiber reinforced–reaction formed SiC matrix composites: Microstructure and interfacial properties

M. Singh and R. M. Dickerson
NYMA, Inc., Lewis Research Center Group, Cleveland, Ohio 44135

Forrest A. Olmstead
Department of Mechanical Engineering, Case Western Reserve University, Cleveland, Ohio 44106

J. I. Eldridge
NASA Lewis Research Center, Cleveland, Ohio 44135

(Received 18 March 1996; accepted 24 November 1996)

Microstructural and interfacial characterization of unidirectional SiC (SCS-6) fiber reinforced–reaction formed SiC (RFSC) composites has been carried out. Silicon–1.7 at.% molybdenum alloy was used as the melt infiltrant, instead of pure silicon, to reduce the activity of silicon in the melt as well as to reduce the amount of free silicon in the matrix. Electron microprobe analysis was used to evaluate the microstructure and phase distribution in these composites. The matrix is SiC with a bi-modal grain-size distribution and small amounts of $MoSi_2$, silicon, and carbon. Fiber push-outs tests on these composites showed that a desirably low interfacial shear strength was achieved. The average debond shear stress at room temperature varied with specimen thickness from 29 to 64 MPa, with higher values observed for thinner specimens. Initial frictional sliding stresses showed little thickness dependence with values generally close to 30 MPa. Push-out test results showed very little change when the test temperature was increased to 800 °C from room temperature, indicating an absence of significant residual stresses in the composite.

I. INTRODUCTION

Recently, there has been a surge of interest in the research and development of silicon carbide-based advanced composites for aerospace and other high-temperature structural applications.[1,2] These composites have low density, high strength and toughness, good oxidation and thermal shock resistance, and high thermal conductivity. In addition to the need to meet design requirements, these composites must be cost effective and affordable for various applications. Fabrication of composite components into near-net and complex shapes significantly reduces the component cost. Currently, silicon carbide matrix composites have been fabricated by a number of techniques: hot pressing,[3,4] polymer pyrolysis,[5] chemical vapor infiltration,[6] and melt infiltration.[7] Material and processing attributes of the above fabrication approaches have been discussed elsewhere.[8] In summary, the majority of composite processing techniques being used to date are either expensive or have limitations in complex shape and near-net-shape fabrication.

In contrast, the reaction forming process has many advantages over the processing techniques described above. In this process, a microporous carbon preform containing fibers is infiltrated with molten silicon or silicon-refractory metal (molybdenum, niobium) alloys.[8–10] The infiltrating materials react with the carbon and form matrices of silicon carbide, refractory disilicides ($MoSi_2$, $NbSi_2$), and silicon. It is also tailorable through control of residual phases (refractory disilicides and silicon). Since the starting material is a liquid polymer, second phases can be incorporated very easily. This processing approach has been used for the fabrication of silicon carbide matrix composites with large diameter monofilament or small diameter fibers.[8–10] The relative amounts of these phases depends on the morphology and porosity of the carbon precursor matrix, reaction conditions, and the composition of the infiltration materials. This process yields composites with full density and is capable of fabricating composite components with near-net and complex shapes.

The objective of this paper is to study the microstructure and interfacial properties of silicon carbide (SCS-6) fiber reinforced–reaction formed silicon carbide matrix composites fabricated by silicon–1.7 at.% molybdenum alloy infiltration. Electron microscopy and microprobe analysis were used to determine the overall microstructure, the distribution of molybdenum disilicide, and to determine whether there was any incorporation of the molybdenum apart from the disilicide. Since the preservation of a relatively low interfacial

shear strength after fabrication by the alloy infiltration process is key to composite performance, fiber push-out tests were performed at room and elevated temperatures in order to evaluate the interfacial mechanical properties.

II. EXPERIMENTAL PROCEDURES

In fabricating the composite matrix, a mixture of furfuryl alcohol resin, diethylene and triethylene glycols, and p-toluene sulfonic acid was used. The SCS-6 fiber tapes were made by winding them on a drum. These tapes were about 3 in. wide (88 fibers/inch) and 6.5 in. long. For the composites reported in this paper, 8 plies of fiber tapes were layed-up in a mold and the resin mixture was poured over it. The mold with the fibers and the resin mixture was cured at 70 °C and then slowly heated up to 700 °C in flowing argon atmosphere. The pyrolysis of the solid polymer with fibers yielded a porous carbonaceous preform. This fiber preform was held in contact with the molten silicon–1.7 at.% molybdenum alloy infiltrant at 1430 °C for 15 min in vacuum. At the infiltration temperature, the molten silicon-molybdenum alloy reacted with the carbon in the preform. Further details of the composite processing are provided elsewhere.[8] The rate of infiltration depends on the wetting of the preform by the melt which increases with increasing temperature. The selection of processing time and temperature is critical for the control of microstructure and interfacial reactions, and these control mechanical properties of the composites.

Cross-sectional samples were metallographically mounted and polished for optical microscopy, scanning electron microscopy (SEM), and electron microprobe analysis (EMPA). SEM was performed on a JEOL JSM 840A and EMPA was done using an ARL SEMQ microprobe. Transmission electron microscopy (TEM) thin foils were prepared using standard techniques. Slices from the composites were diamond sliced 1 mm thick, ultrasonically drilled to a 3 mm diameter, ground, and polished to 80 μm thickness with a 3 μm finish, dimple ground to a center thickness of 30 μm, Ar ion milled until a thin area at fiber/matrix interfaces was achieved, and coated with a thin layer of evaporated carbon prior to examination. TEM was performed with a Philips EM400T operating at 120 keV with a Kevex Quantum thin-window x-ray energy dispersive spectrometer for chemical analysis.

Interfacial mechanical properties were evaluated by fiber push-out tests performed at both room temperature and 800 °C. The room temperature and elevated temperature testing facilities and procedures have been previously described.[11,12] A 112 μm diameter tungsten carbide punch was used to push out the 142 μm diameter SCS-6 fibers that were aligned over grooves (500 μm wide for tests with the room temperature apparatus; 300 μm wide for tests with the elevated temperature apparatus) in the sample support. Acoustic emission was monitored during room temperature tests using a 200 kHz acoustic transducer. Earlier work[13] has shown that the acoustic emission events detected during fiber push-out can be used to identify the occurrence of unstable fiber/matrix debonding.

For this study, specimens ranging in thickness from 0.28 to 1.45 mm were tested. Except where noted otherwise, room temperature tests were performed in room air (25–35% relative humidity), while the 800 °C tests were performed in vacuum (low 10^{-6} Torr range). From eight to ten fibers were pushed out in each sample tested at room temperature, and five to nine fibers were pushed out in each sample tested at 800 °C.

The average interfacial stresses at fiber debonding, τ_{debond}, and for frictional sliding, τ_{friction}, were calculated by simply dividing the applied load by the nominal contact area between the fiber and matrix:

$$\tau = \frac{P}{\pi d_{\text{fiber}} t} \tag{1}$$

where d_{fiber} is the fiber diameter and t is the specimen thickness.

III. RESULTS AND DISCUSSION

A. Microstructure

Figure 1 shows a polished section of the composite formed by the infiltration of the preform with a silicon–1.7 at.% molybdenum alloy. The uniformity of the reaction-formed material reflects the well-controlled porosity of the carbon preform obtainable using the present method.

In order to understand the various aspects of reactive infiltration, i.e., infiltration temperature, infiltrant composition, and phase stabilities in the final material, we need to have information from the phase diagrams of the

FIG. 1. Optical micrograph of composite infiltrated with molten silicon–1.7 at.% Mo alloy.

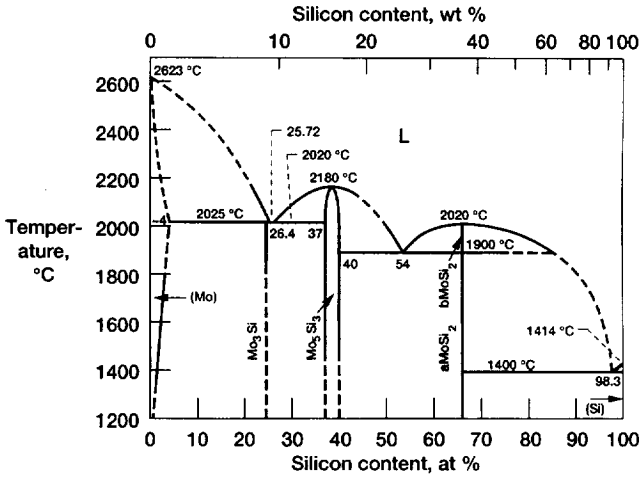

FIG. 2. Phase diagram of molybdenum-silicon system.[14]

molybdenum-silicon (Mo–Si) and molybdenum-silicon-carbon (Mo–Si–C) systems. The phase diagram of the binary molybdenum-silicon system[14] shown in Fig. 2 has a eutectic at the silicon-rich side of the diagram at 1.7 at. % Mo composition and a eutectic temperature of 1400 °C. A large two-phase (liquid silicon and solid molybdenum disilicide) region also exists. Because of the reaction of silicon with carbon during processing, the local concentration of silicon in the alloy melt decreases and the melt composition shifts toward the two-phase region (liquid silicon and molybdenum disilicide) where molybdenum disilicide starts to precipitate from the melt. To achieve high-volume fractions of molybdenum disilicide in the reaction-formed silicon carbide materials, the infiltrant composition and infiltration temperature should be chosen accordingly. Nowotny *et al.*[15] have reported on the high temperature phase diagram of the Mo–Si–C system at 1600 °C. There is a narrow two-phase field that exists between $MoSi_2$ and SiC, indicating mutual stability of these phases at 1600 °C. In addition, there is a three-phase field containing $MoSi_2$, SiC, and Si.

Compositional dot maps of the composite from the electron microprobe (Fig. 3) show that the molybdenum was incorporated in small clusters of particles in the matrix and had not diffused into or reacted with the SCS-6 fibers. The EMPA further revealed that the residual silicon and the $MoSi_2$ were dispersed within the matrix. Higher magnification SEM images of the fiber-matrix interface (Fig. 4) reveal that some regions of the outer carbon-rich coating of the fiber had reacted to form scalloped regions of SiC. These reactions are limited and also strongly depend on the chemistry and morphology of the porous carbon preforms and processing conditions (time and temperature). The liquid resin provided a thin carbon coating on the fibers during composite fabrication. The presence of this thin carbon coating coupled with the well-controlled porosity of the carbon preform was the leading contributor to the significant reduction in the reaction of alloy infiltrants with the fibers during processing and thus avoided extensive fiber damage. In other melt-infiltration-processed composites,[7] various interfacial coatings 4–5 μm thick are required to provide suf-

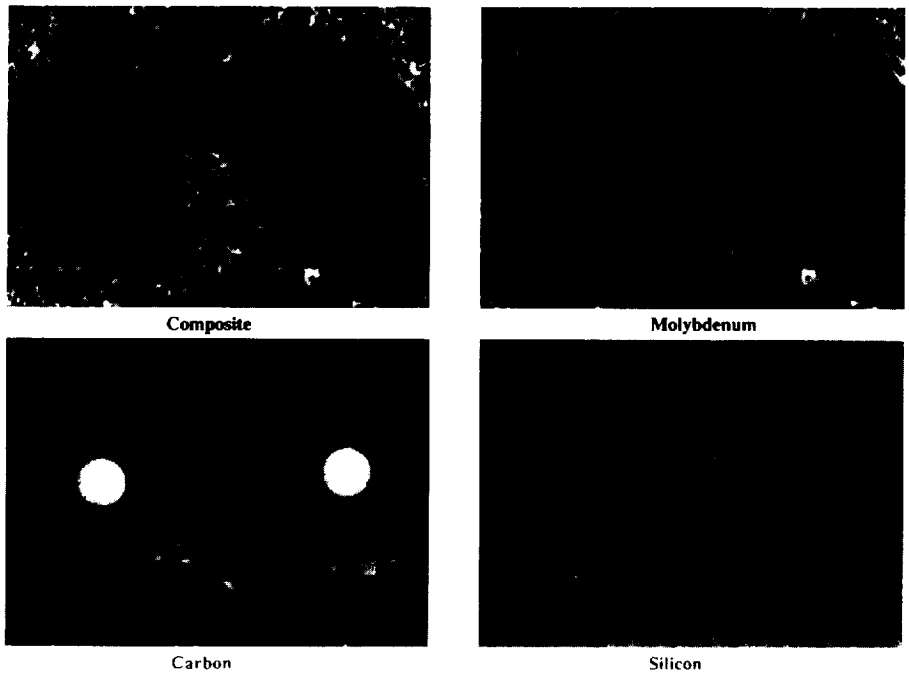

FIG. 3. Electron microprobe images of the composite formed using x-ray signals from molybdenum, carbon, and silicon as well as back-scattered electrons (BSE's).

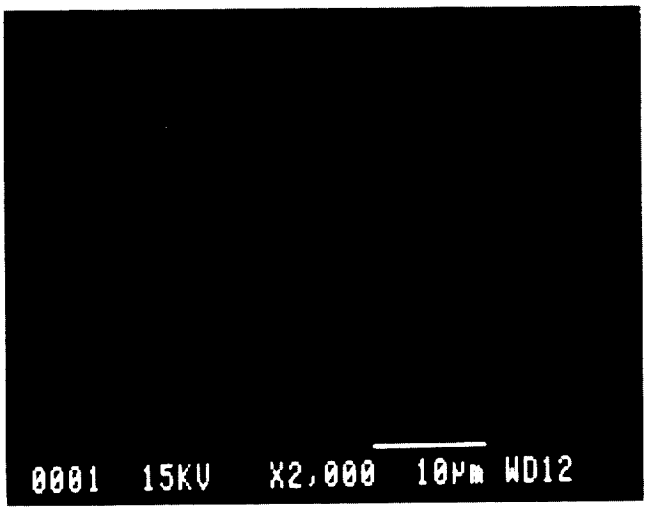

FIG. 4. Scanning electron micrograph of the fiber/matrix interface using BSE contrast showing scalloped reaction region of the outer carbon-rich layer.

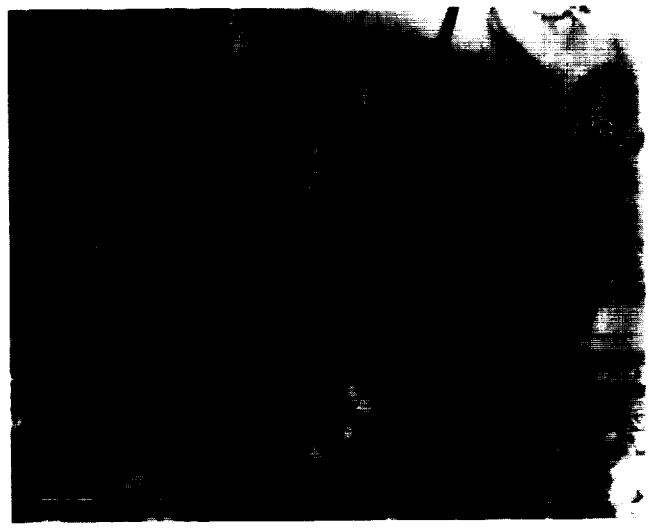

FIG. 5. Transmission electron micrograph (TEM) showing the bimodal and separate SiC grain size distributions.

ficient protection to fibers. In the present approach, the interface between the outer carbon-rich coating layer and the inner carbon-rich coating layer, which is typically the most important feature for fiber pullout and composite-like behavior, was seldom disturbed. The somewhat convoluted matrix-coating interface produced by uneven reaction of the outer coating with the matrix makes that interface more resistant to sliding than either the fiber-coating or internal-coating interface. This feature is evidenced by the observed locations of interfacial debonding produced by fiber push-out (see Sec. III. C).

B. TEM analysis

The reaction-formed silicon carbide matrix immediately surrounding the outer carbon-rich coatings of the fiber was seen in the TEM to be primarily fine-grained SiC. These interfacial regions often extended somewhat into the outermost carbon-rich layer of the SCS-6 fibers, as was also observed via SEM (Fig. 4). However, the interface between the two carbon layers in the fiber coating was almost always intact. This is important because this relatively weak interface allows fiber pullout, which toughens the composite during fracture. Immediately outside the fine SiC layer, one may find any of the matrix phases. TEM of the matrix confirmed the presence, crystallographically and compositionally, of SiC, $MoSi_2$, Si, and C.

The SiC was observed to have a bimodal distribution of grain sizes. The finer SiC regions consist of grains between 30 nm and 1 μm in size. Coarser SiC regions, generally having particles between 1 and 5 μm in diameter, were also observed (Fig. 5). Comparisons of these results with SEM backscattered electron images of the TEM thin foils showed that the finer SiC clusters were slightly higher in average atomic number. This suggests that these areas may contain some residual intergranular Si, which was not readily observable. No Mo was detected via EDS in the finer SiC. While occasional, weak "extra" reflections were observed in selected area diffraction patterns taken from the fine SiC, they were too dim to be observed *in situ*. Electron diffraction patterns from several SiC grains showed the majority to be the cubic β polytype, but some grains were hexagonal 6H in structure.

Both $MoSi_2$ and Si grains were relatively large and featureless. The residual C was observed to be fibrous, yielding diffraction patterns consistent with a turbostratic structure. These observations are quite similar to those reported earlier in a similar composite containing $NbSi_2$.[10]

C. Interfacial shear strengths

As was mentioned earlier, the silicon carbide (SCS-6) fiber used in this study has an outer carbon-rich coating applied by the manufacturer. In a brittle fiber-brittle matrix composite, a low-shear-strength material must separate the fiber and matrix to achieve a tough composite. The coating on the SCS-6 fiber has been shown in the past to exhibit desirably low interfacial shear strengths within the coating and between the coating and fiber in a ceramic matrix.[16] Results of the fiber push-out tests reported here confirm that this beneficial low interfacial shear strength is maintained after the reaction-forming process using the molten silicon-molybdenum alloy infiltration.

Table I summarizes the results of all the push-out tests performed at room temperature and 800 °C. Figure 6(a)–6(c) shows typical room-temperature fiber

TABLE I. Summary of fiber push-out test results.

Thickness (mm)	Temp.	$P_{\text{initial debond}}$ (N)	$P_{\text{final debond}}$ (N)	P_{friction} (N)	$\tau_{\text{final debond}}$ (MPa)	τ_{friction} (MPa)
0.28	RT	8.04 ± 2.40	8.04 ± 2.40	3.82 ± 1.06	64.39 ± 19.18	30.62 ± 8.48
0.34	RT	8.76 ± 2.54	8.76 ± 2.54	4.71 ± 1.75	57.78 ± 16.74	31.05 ± 11.57
	800 °C	7.69 ± 2.29		5.94 ± 1.98		39.19 ± 13.04
0.67	RT	10.07 ± 2.52	11.20 ± 2.92	9.85 ± 2.56	37.46 ± 9.77	32.97 ± 8.56
	800 °C		12.21 ± 2.15	11.10 ± 2.02	40.86 ± 7.20	37.13 ± 6.77
1.20	RT	8.16 ± 2.00	15.33 ± 4.53	15.26 ± 5.29	28.63 ± 8.47	28.50 ± 9.89
	800 °C		22.24 ± 1.38	21.64 ± 1.39	41.55 ± 2.57	40.43 ± 2.59
1.45	RT	19.04 ± 3.71	30.34 ± 9.80	27.77 ± 8.09	46.91 ± 15.15	42.93 ± 12.51

push-out load-displacement curves (displacement measured by a capacitance displacement gauge), along with the amplitude of detected acoustic emission, for a range of specimen thicknesses. While the thinnest sample, Fig. 6(a), shows a single debonding (sharp load decrease after debonding load P_{debond}) with a simultaneous acoustic emission spike, the thicker specimens, Figs. 6(b) and 6(c) show incremental or progressive debonding. This type of progressive debonding has been observed before for SCS-6/RBSN composites.[16,17] Debond initiation occurs where the load-displacement curve deviates from its initially linear slope (with simultaneous acoustic emission spike). The initial debonding represents debond initiation, and the initial debonding loads ($P_{\text{initial debond}}$) are given in Table I. After initial debonding, the load-displacement curve continues with a lower slope until a load decrease (simultaneous with a second acoustic emission spike) occurs. This second debonding event [Figs. 6(b) and 6(c)], which becomes less pronounced for thicker specimens, corresponds to completion of fiber

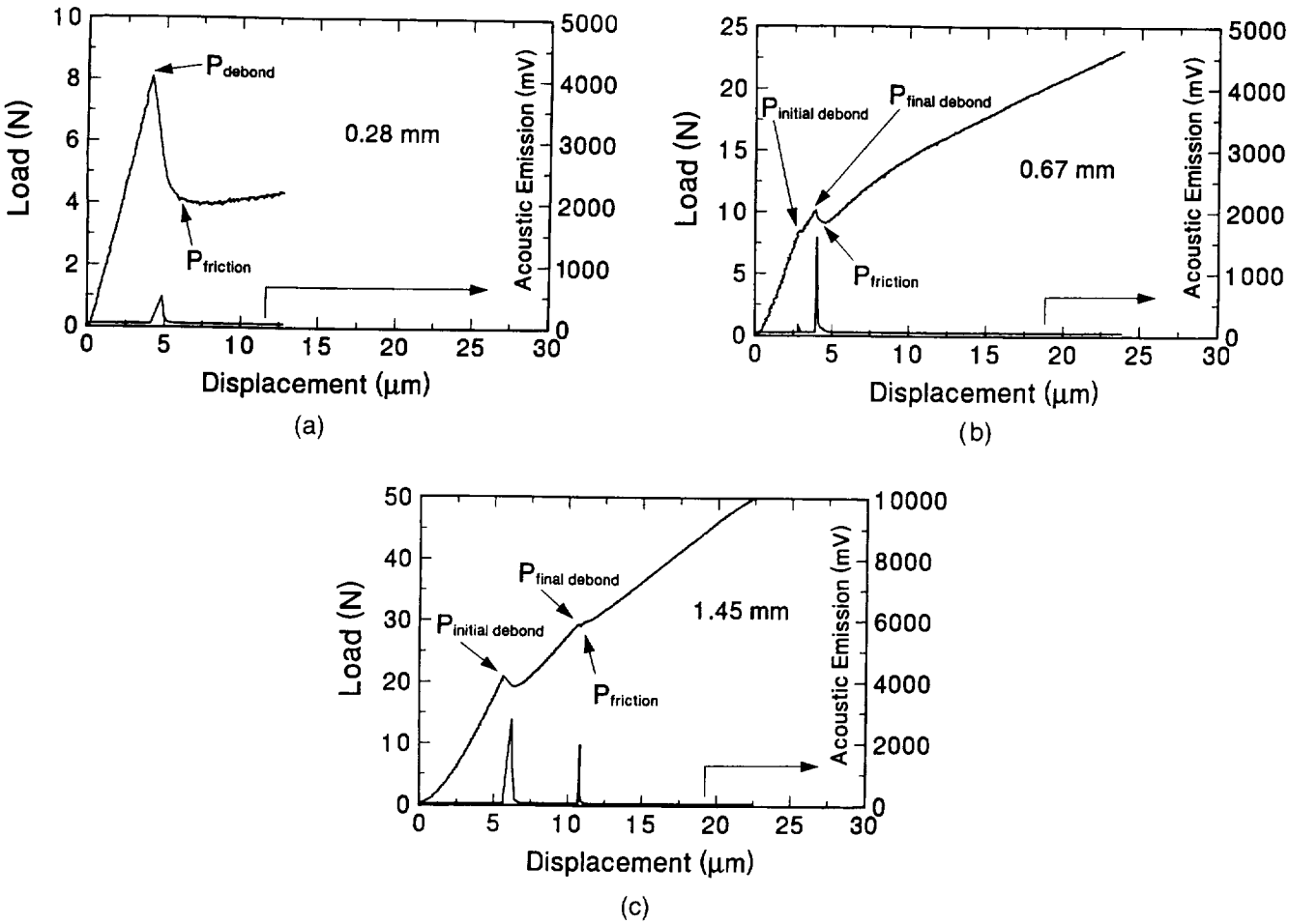

FIG. 6. Load-displacement behavior during room temperature fiber push-out tests: (a) 0.28 mm, (b) 0.67 mm, and (c) 1.45 mm thick specimens.

debonding; this is when interfacial debonding has propagated to the bottom of the sample, allowing the whole fiber to move. The load measured at this final debonding was selected as the debonding load, $P_{\text{final debond}}$. In all cases, the frictional sliding load, P_{friction}, was selected to be the load attained immediately after the sharp load decrease occurring upon final debonding. The observed significant changes in frictional resistance with continued fiber sliding were not addressed in this study.

The dependence of the average final debonding and frictional sliding stresses on specimen thickness is illustrated in Figs. 7(a) and 7(b). The average τ_{debond} values at room temperature [Fig. 7(a)] showed significant variation from 29 to 64 MPa with the higher values observed for the thinner specimens. The τ_{debond} has been used for final debond stress in further discussions. The average τ_{friction} values showed much less variation with sample thickness with most of the room temperature values close to 30 MPa [Fig. 7(b)]. The apparent thickness dependence of τ_{debond} may be the result from the oversimplistic application of Eq. (1); as the specimen thickness is varied, the debonding process changes from a single debonding to progressive debonding with partial fiber sliding. Thus, P_{debond} includes contributions from both frictional resistance to sliding and debonding strength or fracture energy. The relative weight of these contributions will change with specimen thickness, so that normalizing to specimen thickness as in Eq. (1) should not be expected to be valid over a wide range of specimen thicknesses. While the τ_{debond} values calculated using Eq. (1) are useful for comparison, they are average stresses (over the length of the interface), and do not represent the actual (local) shear strength of the interface. In contrast, τ_{friction} values determined using Eq. (1) are consistent over a wide range of specimen thickness. In this case, Eq. (1) is a good approximation because when the entire fiber is moving, the resistance to fiber movement is purely frictional and the interfacial shear stress is fairly uniform over the length of the interface.

The temperature dependence of the fiber debonding and sliding stresses are shown in Figs. 8(a) and 8(b).

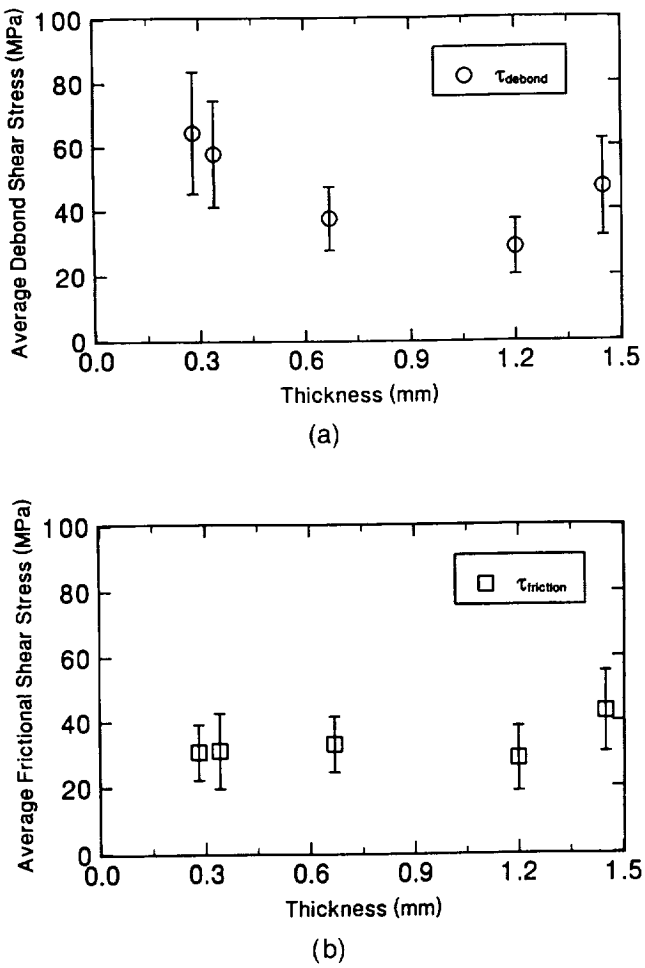

FIG. 7. Effect of specimen thickness on the (a) debond and (b) frictional sliding stresses in composites at room temperature in room air.

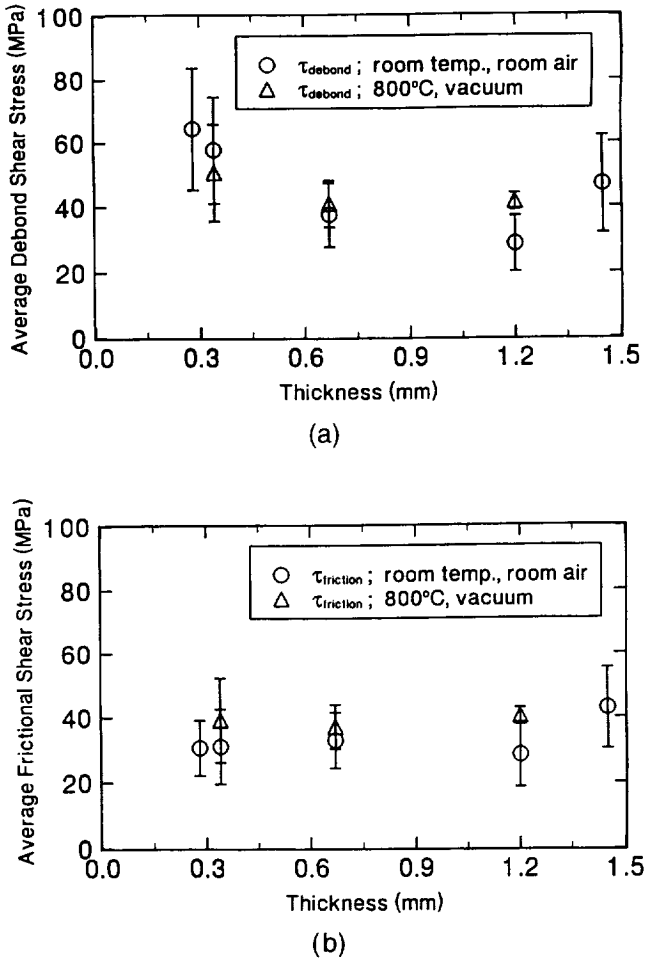

FIG. 8. Effect of specimen thickness on the (a) debond and (b) frictional sliding stresses in composites at 800 °C in vacuum.

There was very little change in either τ_{debond} or $\tau_{friction}$ when the testing temperature was increased from room temperature to 800 °C. Although the test environments at room temperature and 800 °C were different, other work[18] has shown that the change in environment did not significantly affect τ_{debond} and initial $\tau_{friction}$. Therefore, the lack of significant change in τ_{debond} and $\tau_{friction}$ with temperature suggests the absence of significant residual stresses within the composites. In contrast, significant changes in τ_{debond} and $\tau_{friction}$ were observed in other SiC (SCS-6) fiber-reinforced composites where there were significant differences in thermal expansion coefficients between the SCS-6 fiber and matrix.[19]

Figures 9(a)–9(d) show typical micrographs of fibers pushed out at room temperature. Two locations for interfacial failure were observed. The majority of fibers debond between the outer carbon layers of the SiC (SCS-6) fibers [Figs. 9(a) and 9(b)] with some debonding occurring between the fiber and its carbon layers [Figs. 9(c) and 9(d)]. Failure was never observed at the coating-matrix interface, which was much rougher than the interfaces where failure was observed.

IV. CONCLUSIONS

The findings of this microstructural and mechanical property study suggest that SiC (SCS-6) fiber reinforced–reaction formed silicon carbide matrix composites can be fabricated by the reaction-forming process without the need for any additional interface coating on the SCS-6 fibers. Minimal damage to the fiber coating has been attributed to the microstructural uniformity of the precursor carbon matrix in the preform. This allows the majority of the inherently weak SCS-6

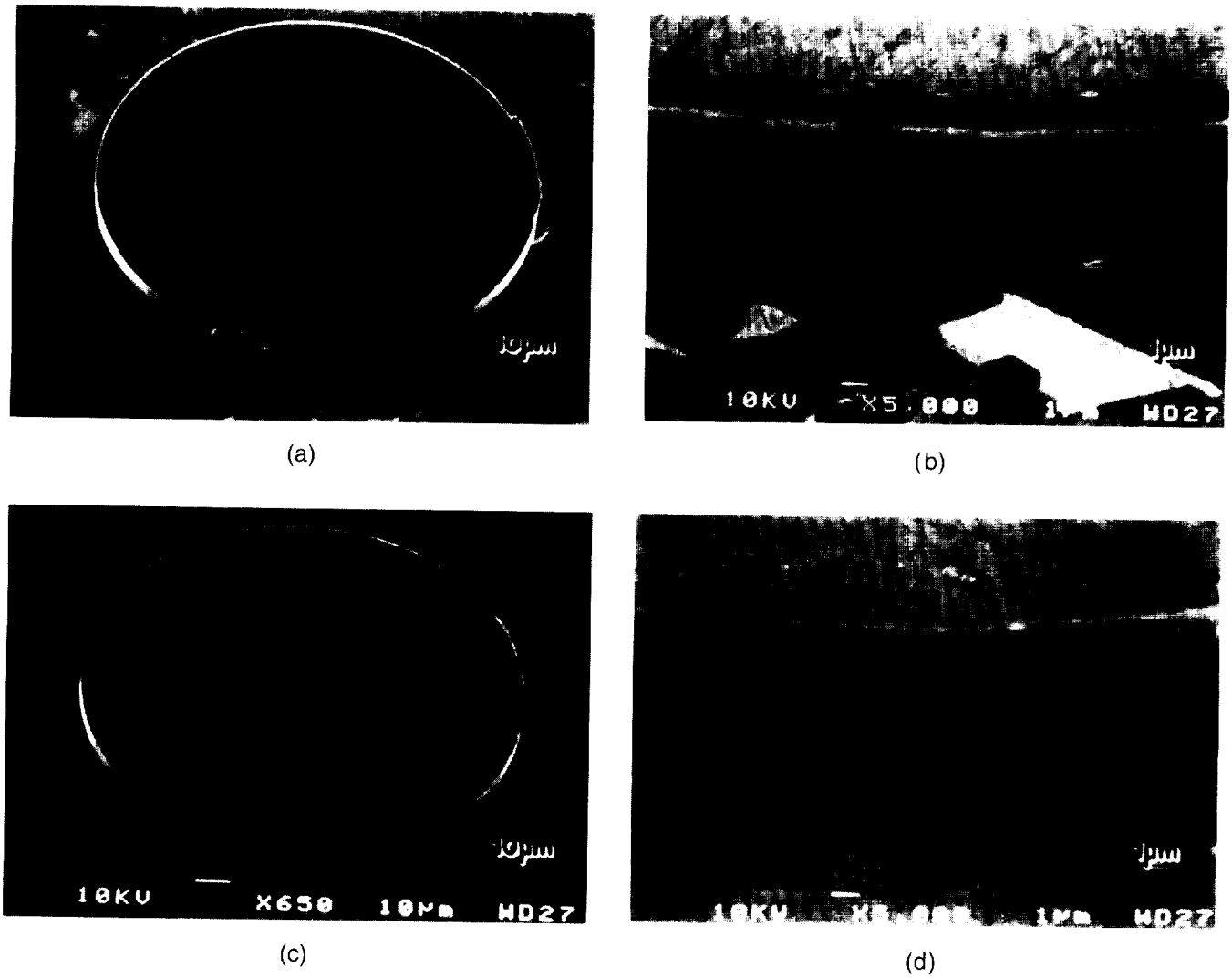

FIG. 9. Micrographs showing typical failure modes in push-out tests: (a, b) between coating layers and (c, d) between fiber and inner coating layers.

coating layers to be preserved and allows for debonding within the coating or between the coating and the fiber. The microscopic and EMPA results indicate that the molybdenum from the silicon-molybdenum alloy precipitates as molybdenum disilicide ($MoSi_2$) in the matrix. The silicon carbide matrix shows a bi-modal-grain-size distribution with grain sizes in the range of 1–5 μm (large grains) and approximately 30 nm to 1 μm (small grains). Results from push-out tests performed at 800 °C were very similar to the results of room-temperature tests, indicating an absence of significant residual stresses in these composites.

ACKNOWLEDGMENTS

We wish to thank Mr. R.F. Dacek, Frank Terepka, Todd Leonhardt, and A. Korenyi-Both for their help in the experimental work.

REFERENCES

1. E. Fitzer and R. Gadow, Am. Ceram. Soc. Bull. **65** (2), 325–335 (1986).
2. D.C. Larsen, J. Adams, L. Johnson, A. Teotia, and L. Hill, *Ceramic Materials for Heat Engines* (Noyes Publications, Park Ridge, NJ, 1985).
3. H. Kodama, H. Sakamoto, and T. Miyoshi, J. Am. Ceram. Soc. **72** (4), 551–558 (1989).
4. T. Miyoshi, H. Kodama, H. Sakamoto, A. Gotoh, and S. Iijima, Metall. Trans. **20A** (11), 2419–2423 (1989).
5. F.I. Hurwitz, NASA-TM 105754 (1992).
6. P.J. Lamicq, G.A. Bernhart, M.M. Dauchier, and J.G. Mace, Am. Ceram. Soc. Bull. **65** (2), 336–338 (1986).
7. K. Luthra, R.N. Singh, and M. Brun, in *High Temperature Ceramic Matrix Composites*, edited by R. Naslain, J. Lamon, and D. Doumeingts (Woodhead Publishing Ltd., 1993), pp. 429–436.
8. M. Singh and S.R. Levine, NASA TM-107001 (1995).
9. M. Singh, unpublished work (1996).
10. M. Singh and R.M. Dickerson, J. Mater. Res. **11**, 746–751 (1996).
11. J.I. Eldridge, NASA-TM-105341 (1991).
12. J.I. Eldridge and B.T. Ebihara, J. Mater. Res. **9**, 1035–1042 (1994).
13. J.I. Eldridge and P.K. Brindley, J. Mater. Sci. Lett. **8** (12), 1451–1454 (1989).
14. *Handbook of Binary Alloy Phase Diagrams* (American Society for Metals, Materials Park, OH, 1990).
15. H. Nowotny, E. Parthé, R. Kieffer, and F. Benesovsky, Monatsch. Chem. **85**, 255 (1954).
16. J.I. Eldridge, R.T. Bhatt, and J.D. Kiser, Ceram. Eng. Sci. Proc. **12**, 7–8, 1152–1171 (1991).
17. A. Dollar and P.S. Steif, J. Am. Ceram. Soc. **76** (4), 897–903 (1993).
18. M. Singh and J.I. Eldridge, unpublished work (1996).
19. J.I. Eldridge, in *Ceramic Matrix Composites—Advanced High-Temperature Structural Materials*, edited by R.A. Lowden, J.R. Hellmann, M.K. Ferber, S.G. DiPietro, and K.K. Chawla (Mater. Res. Soc. Symp. Proc. **365**, Pittsburgh, PA, 1995), pp. 283–290.